Charge-Orbital Density Wave and Superconductivity in the Strong Spin-Orbit Coupled IrTe_{2}:Pd

J. J. Yang, Y. J. Choi, Y. S. Oh, A. Hogan, Y. Horibe, K. Kim, B. I. Min, and S-W. Cheong

Phys. Rev. Lett. **108**, 116402 — Published 13 March 2012

DOI: 10.1103/PhysRevLett.108.116402

Charge/orbital density wave and superconductivity in the strong spin-orbit coupled $IrTe_2$:Pd

J. J. Yang[1,2], Y. J. Choi[3], Y. S. Oh[3], A. Hogan[3], Y. Horibe[3], K. Kim[2], B. I. Min[2], and S-W. Cheong[1,2,3,a]

[1] Laboratory for Pohang Emergent Materials, Pohang University of Science and Technology, Pohang 790-784, Korea

[2] Department of Physics, Pohang University of Science and Technology, Pohang 790-784, Korea

[3] Rutgers Center for Emergent Materials and Department of Physics & Astronomy, Rutgers University, Piscataway, NJ 08854, USA

Using transmission electron microscopy, the anomalies in resistivity and magnetic susceptibility at ~262 K in $IrTe_2$ are found to accompany the superlattice peaks with $\vec{q}$=(1/5, 0, -1/5). The wave vector is consistent with our theoretical calculation for the Fermi surface nesting vector, indicating that the ~262 K transition is charge/orbital density wave (DW)-type. We also discovered that both Pd intercalation and substitution induce bulk superconductivity with T_c up to ~3 K, which competes with DW in a quantum critical point-like manner.

PACS numbers:

a) Electronic mail: sangc@physics.rutgers.edu

Materials with large spin-orbital (SO) coupling have induced phenomenal attraction in condensed matter physics and materials science communities. Large SO coupling is prerequisite for hard magnets (such as $SmCo_5$ [1] and FePt [2]) with large magnetic anisotropy [3] or multiferroics (such as orthorhombic $HoMnO_3$ [4]) with large magnetism-induced polarizations [5]. Furthermore, large SO coupling can result in unique quantum states such as J_{eff}=1/2 Mott insulators such as Sr_2IrO_4 where spin and orbital degrees of freedom are strongly entangled [6] or topological insulators such as Bi_2Se_3 and Bi_2Te_3 [7,8]. Topological insulators are materials with finite band gaps in which large SO coupling induces band inversion, so topological metallic surface states with Dirac cone-like dispersions, protected by time reversal symmetry, appear [9-11]. Furthermore, non-conventional superconductivity pairing can be present in the so-called topological superconductors with large SO coupling [12-14]. Cu-intercalated Bi_2Se_3 ($Cu_xBi_2Se_3$) is a candidate for the topological superconductors [15-19]. It will be highly valuable to discover new superconductors with large SO coupling in order to understand the nature of topological superconductivity. Note that SO coupling is proportional to Z^4 where Z is the atomic number, and further exploration of materials with large Z's may lead to new quantum states or novel functionalities.

Due to large Z, $IrTe_2$ must be associated with huge SO coupling, which is expected to be comparable with that of topologically-insulating Bi_2Se_3. Interestingly, $IrTe_2$ exhibits an intriguing phase transition at ~250 K where distinct anomalies of resistivity and magnetic susceptibility were observed [20], but the exact nature of the transition has been little studied. We discovered that the phase transition is charge/orbital density wave (DW)-type, and superconductivity with T_c up to ~3 K sets in as soon as the DW transition is suppressed by intercalation (Pd_xIrTe_2) or Ir-site doping ($Ir_{1-y}Pd_yTe_2$) of a small amount of Pd. We emphasize that both Pd_xIrTe_2 and $Ir_{1-y}Pd_yTe_2$ near the optimal concentrations exhibit full magnetic shielding below T_c, and complete superconducting transitions in resistance-temperature curves, indicating bulk intrinsic superconductivity. On the contrary, $Cu_xBi_2Se_3$, a candidate for the topological superconductors, tends to show a poor superconducting transition [15-17]. Thus, Pd_xIrTe_2 and $Ir_{1-y}Pd_yTe_2$ may be better systems to explore the possibility of topological superconductivity.

Polycrystalline specimens of Pd_xIrTe_2 and $Ir_{1-y}Pd_yTe_2$ were prepared using 99.95 % Ir, 99.99 % Te and 99.99 % Pd. Stoichiometric quantities of the elements were mixed, ground and pelletized. Then, the pellets were placed in quartz tubes and sealed under vacuum. The pellets were sintered at 1000 °C for 15 hours, followed by furnace cooling to room temperature. The process was repeated twice with an intermediate grinding. The results of x-ray diffraction (XRD), performed using a Rigaku D/max-RB x-ray diffractometer with a Cu K_α radiation, show that all specimens are in single phase. Magnetic and electrical transport properties were measured using the Quantum design MPMS-XL7 and PPMS-9. The specimens for the TEM experiments were prepared with gentle crushing of the pellets. The observations were carried out with the JEOL-2010F and JEOL-2000FX transmission electron microscopes (TEM) equipped with a liquid-nitrogen-cooled holder. The structural change in $IrTe_2$ was investigated with observing electron diffraction (ED) patterns upon cooling. Note that the indexes in the ED patterns are based on the trigonal structure.

$IrTe_2$ is a layered compound with trigonal symmetry ($P\bar{3}m1$) as shown in Fig. 1 (a). Ir ions are octahedrally coordinated with six Te ions, and face sharing of Ir-Te_6 cages forms $IrTe_2$ layers. Different from typical layered transitional metal dichalcogenides, $IrTe_2$ layers are bonded to each other by significant “Te-Te bonding”, rather than weak van der Waals force [21]. However, the $IrTe_2$ crystals are highly cleavable along $IrTe_2$ layers, and Pd ions can be intercalated between $IrTe_2$ layers (see the schematics of the intercalated Pd ions in the left panel of Fig. 1(a)). This results in a monotonic increase of the *c* lattice parameter with increasing Pd content in Pd_xIrTe_2 as evinced by our refined lattice parameters (see S1 of SI) [22]. For Pd substituted $Ir_{1-y}Pd_yTe_2$, a part of Ir ions in $IrTe_2$ layer are replaced by Pd ions. Considering the fact that the *a* lattice parameter of $PdTe_2$ (4.034 Å) is larger than that of $IrTe_2$ (3.930 Å) and the *c* lattice parameter of $PdTe_2$ (5.132 Å) is smaller than that of $IrTe_2$ (5.386 Å), Pd substitution into $IrTe_2$ will result in the increase of *a* and decrease of *c* [23], consistent with our refinement results of $Ir_{1-y}Pd_yTe_2$ (S1 of SI).

Figure 1(b) and (c) show the temperature dependence of magnetic susceptibility

and resistivity for Pd_xIrTe_2. Consistent with previous reports, pure $IrTe_2$ exhibits a 200-280 K transition with a large thermal hysteresis accompanying a magnetic susceptibility drop and resistivity increase upon cooling. When 2 % Pd is intercalated into $IrTe_2$, the transition is significantly suppressed to 120-190 K, and the magnitude of the magnetic susceptibility drop decreases. For 3 % Pd intercalation, a hint of the transition exists at 70-150 K, and the transition appears to be absent at 4 % Pd intercalation. Fig. 1(d) and Fig. 1(e) exhibit the temperature dependence of magnetic susceptibility and resistivity for doped $Ir_{1-y}Pd_yTe_2$. Pd substitution suppresses the transition in a manner slightly slower than that for Pd intercalation. For y=0.03, the transition is suppressed to 130-180 K, and is not visible at y=0.05. A sudden increase of resistivity exists at the transition, but the temperature dependence below the transition temperature remains metallic, suggesting that a partial gap opens at the Fermi level below the transition.

The resistivity and magnetic susceptibility behavior at the transition in $IrTe_2$ is reminiscent of the formation of charge DW [20]. Nevertheless, the result of an NMR experiment did not provide any evidence for charge DW order [24]. Matsumoto *et al.* proposed that the transition is due to the crystallographic deformation from high temperature $P\bar{3}m1$ to low temperature *C*2/*m* [20]. In order to clarify the origin of the transition, ED experiments were performed at low temperatures. Figure 2(a) shows an ED pattern of $IrTe_2$ taken at ~284 K above the transition. The peaks in Fig. 2(a) are consistent with the fundamental reciprocal lattice of the trigonal structure. Figure 2(b) displays an ED pattern with the electron incidence parallel to the $[\bar{1}01]$ direction taken at 84 K below the transition. Superlattice peaks are clearly visible in the 84 K pattern, and indicate the presence of a new structural modulation with the wave vector of $\vec{q}$=(1/5, 0, -1/5) below the transition. The schematics of the new modulation wave vectors and fundamental reciprocal lattice are displayed in Fig. 2(c).

In order to unveil the origin of the new structural modulation, we have calculated the charge susceptibility $\chi(\vec{q})$:

$$\chi(\vec{q}) = \frac{1}{N}\sum_{\vec{k},n,m} \frac{f(\varepsilon_n(\vec{k}))(1-f(\varepsilon_m(\vec{k}+\vec{q})))}{\varepsilon_m(\vec{k}+\vec{q})-\varepsilon_n(\vec{k})+i\delta}$$

The electronic structure of $IrTe_2$ for our calculation was investigated employing the full-potential linearized augmented plane wave (FLAPW) band method implemented in Wien2k code [25]. In addition, the generalized gradient approximation (GGA) was adopted for the exchange correlation potential, and the spin-orbit interaction of Ir and Te ions were included in a second variation manner. As shown in Fig. 2(d), the charge susceptibility along Γ(0, 0, 0)- L'(1/2, 0, -1/2) exhibits the dominant peak at ~2.2/5 of the Γ- L' length, corresponding to the wave vector of $\vec{q}$=(~1.1/5, 0, ~-1.1/5). This indicates the presence of Fermi surface (FS) nesting at $\vec{q}$=(~1.1/5, 0, ~-1.1/5) (see S2 in SI), which is close to the observed superlattice peak position of $\vec{q}$=(1/5, 0, -1/5). The small difference may originate from the commensurability effect when lattice is involved. As comparison, the charge susceptibility calculated without SO coupling is also shown in Fig. 2(d). $\chi(\vec{q})$ without SO coupling also exhibits a dominant peak at $\vec{q}$=(~1.1/5, 0, ~-1.1/5), but the intensity of it is slightly higher than that with SO coupling. Hence, SO coupling suppress slightly the Fermi surface instability, but does not change the wave vector. Furthermore, in materials with partially filled t_{2g} (see S2 of SI) levels such as $IrTe_2$, orbital degree of freedom is intricately coupled with charge degree of freedom, and orbitally-driven Peierls instability can be responsible for a charge DW-type transition [26]. Furthermore, orbital degree of freedom may also contribute to the commensurate locking of the superlattice modulation. Therefore, it may be legitimate to call the transition as a charge/orbital DW order. It is also noteworthy that FS of $IrTe_2$ plotted in Figs. 2(e) and (f) reveals rich dispersions along the *c* direction, reflecting three dimensional (3D) nature of the electronic structure. This 3D nature is consistent with our result of the partial density of states of $IrTe_2$ (see S2 of SI).

We found that superconductivity emerges below ~3 K as soon as the DW transition is suppressed with Pd intercalation or doping, while pure $IrTe_2$ does not show superconductivity down to 0.32 K [27]. This trend is demonstrated in the low-temperature magnetic susceptibility and resistivity data shown in Fig. 3. For x=0.02, diamagnetism appears below ~2.2 K (Fig 3(a)), suggesting the onset of superconductivity. Consistently, resistivity of this sample decreases smoothly to zero

around this temperature (Fig. 3(b)), suggesting bulk superconductivity. For x=0.03, the bulk superconductivity is evident in the full shielding diamagnetic signal and sharp resistivity transition at 2.68 K. With further Pd intercalation, superconducting temperature (T_c) decreases, and superconductivity is no longer detectable at x=0.1. Pd doping in $Ir_{1-y}Pd_yTe_2$ induces a similar trend of superconducting T_c, but at higher Pd concentrations. Weak superconductivity appears at y=0.03, bulk superconductivity is optimized with T_c=2.99 K at y=0.04, and superconducting T_c decreases with further doping beyond y=0.04 (Fig. 3(c) and (d)). Note that the magnetization data in Fig. 3 (a) and (c) are after correcting the demagnetization factor of each specimen. Both intercalated and substituted specimens with nearly optimal compositions exhibit large shielding fraction of ~100%, but Meissner fractions (i.e., field-cooled (FC) magnetization) of all specimens are negligibly small, indicating the presence of bulk superconductivity and also strong superconducting vortex pinning. For comparison, the reported largest shielding fraction of $Cu_xBi_2Se_3$ is only around 40% [17]. In order to reveal the detailed nature of superconductivity, magnetic hysteresis loops of x=0.03 and y=0.05 were measured at 2.0 K and 1.8 K, respectively (Fig. 3(e) and Fig. 3(f)). Both intercalated and substituted specimens exhibit a typical type-II superconductivity behavior. The Ginzburg-Landau parameter κ can be estimated from the following two equations: $-\int MdH = H_c^2/8\pi$ and $H_{c2} = \sqrt{2}\kappa H_c$, where M is diamagnetic magnetization, H is magnetic field, H_c is the thermodynamic critical field and H_{c2} is the upper critical field. From integration of initial magnetization curves and the two equations above, we obtain $\kappa \approx 1.53$ for x=0.03 and $\kappa \approx 1.5$ for y=0.05 [28]. The sharp steps of magnetization near ±0.25 kOe in Fig. 3(f) indicate the presence of avalanche-type flux jumps. Note that because of the polycrystalline nature and expected poor thermal conductivity of our specimens due to the presence of heavy ions such as Ir and Te, the flux jumps can be accompanied with local heating [29].

Our results are summarized in the electronic phase diagram presented in Fig. 4. The DW transition temperature in $IrTe_2$ is strongly suppressed with Pd intercalation or substitution. As soon as DW order is significantly suppressed, superconductivity appears. The superconducting state appears for $x \geq 0.02$ (intercalation) and $y \geq 0.03$ (substitution), and superconducting T_c becomes the maximum of 2.68 K at x=0.03 and of 2.99 K at y=0.04, followed by T_c reduction for higher Pd concentrations.

$Pd_{0.1}$-intercalated $IrTe_2$ is not superconducting down to 1.8 K. But, $Pd_{0.1}$-substituted $IrTe_2$ is still superconducting at T_c≈2.3 K, which appears consistent with the superconductivity of $PdTe_2$ at T_c≈1.69 K [27]. It is plausible that superconductivity and DW order coexist at x=0.02 and y=0.03 in a spatially-inhomogeneous manner. A similar dome-like shape of superconducting phase boundary, where another long-range order disappears, has been observed in a number of systems including superconducting cuprates and Cu_xTiSe_2 [22, 30]. Barath *et al.* proposed that the dome-like shape of T_c(x) and superconducting paring mechanism in Cu_xTiSe_2 stem from quantum criticality associated with fluctuations of DW order [31, 32]. A similar mechanism may be active in Pd_xIrTe_2 and $Ir_{1-y}PdyTe_2$. We also note that primarily due to large SO coupling, non-conventional superconductivity and also the presence of Majorana surface state have been proposed in $Cu_xBi_2Se_3$ [15, 18, 33]. Since $IrTe_2$:Pd system is expected to have a large SO coupling similar with that in $Cu_xBi_2Se_3$, it is quintessential to explore the possible presence of non-conventional quantum states in $IrTe_2$:Pd .

In conclusion, our results of the low-temperature TEM experiment and theoretical calculation indicate that the phase transition ~262 K in $IrTe_2$, exhibiting a sudden increase of resistivity and a drop of magnetic susceptibility upon cooling, is charge/orbital DW-type. We discovered that bulk intrinsic superconductivity appears when DW order is suppressed with Pd intercalation or doping [34]. Superconductivity and DW order compete in a quantum critical point-like manner. Our findings reveal rich quantum nature of 5d transition metal materials with partially filled t_{2g} levels and large SO coupling and provide better systems for the exploration of topological superconductors.

We thank T. Ozaki and S. Mori (Osaka Prefecture University) for the TEM analysis. BIM and KK acknowledge the supports from the NRF (No. 2009-0079947, No. 2011-0025237). The work at Rutgers was supported by the NSF under Grants No. DMR-1104484.

References

[1] P. Larson, I. I. Mazin and D. A. Papaconstantopoulos, Phys. Rev. B **67**, 214405 (2003).

[2] I. V. Solovyev, P. H. Dederichs and I. Mertig, Phys. Rev. B **52**, 13419 (1995)

[3] J. H. Van Vleck, Phys. Rev **52**, 1178 (1937).

[4] N. Lee *et al*., Phys. Rev. B **84**, 020101 (R) (2011).

[5] S. W. Cheong and M. Mostovoy, Nature. Mater **6**, 13 (2007).

[6] B. J. Kim *et al*., Phys. Rev. Lett **101**, 076402 (2008).

[7] Y. Xia *et al*., Nature Phys **5**, 398 (2009).

[8] H. Zhang *et al*., Nature Phys **5**, 438 (2009).

[9] M. Z. Hasan, and C. L. Kane, Rev. Mod. Phys **82**, 3045 (2010).

[10] J. E. Moore, Nature **464**, 194 (2010).

[11] X. L. Qi and S. C. Zhang, Rev. Mod. Phys **83**, 1057 (2011).

[12] A. P. Schnyder *et al*., Phys. Rev. B **78**, 195125 (2008).

[13] X. L. Qi *et al*., Phys. Rev. Lett. **102**, 187001 (2009)

[14] J. Linder *et al*., Phys. Rev. Lett **104**, 067001 (2010).

[15] Y. S. Hor *et al.*, Phys. Rev. Lett **104,** 057001 (2010).

[16] L. A. Wray *et al*., Nature Phys **6**, 855 (2010).

[17] M. Kriener *et al*., Phys. Rev. Lett **106**, 127004 (2011).

[18] L. Fu, and E. Berg, Phys. Rev. Lett **105**, 097001(2010).

[19] M. Kriener *et al.*, Phys. Rev. Lett **106**, 127004 (2011).

[20] N. Matsumoto *et al.*, J. Low. Temp. Phys **117**, 1129 (1999).

[21] C. S. Lee, and G. J. Miller, Inorganic Chemistry **38**, 5139 (1999).

[22] E. Morosan *et al.*, Nature Phys **2**, 544 (2006).

[23] T. R. Finlayson, W. Reichardt, and H. G. Smith, Phys. Rev. B **33**, 2473 (1986).

[24] K. Mizuno *et al.*, Physica B **312**, 818 (2002).

[25] P. Blaha *et al.*, *WIEN2k, An Augmented Plane Wave Local Orbitals Program for Clculating Crystal Properties* (Karlheinz Schwarz, Techn. Universitat Wien, Austria.

[26] D. I. Khomskii and T. Mizokawa, Phys. Rev. Lett **94**, 156402 (2005)

[27] CH. J. Raub *et al.*, J. Phys. Chem. Solids **26**, 2051 (1965).

[28] M. Tinkham, *Introduction to superconductivity*, 2nd ed. (MGH, New York, 1996).

[29] Jae-Yeap Lee *et al.*, J. Appl. Phys **108**, 033909 (2010).

[30] P. A. Lee, N. Nagaosa and X-G. Wen, Rev. Mod. Phys **78**, 17 (2006)

[31] H. Barath *et al.*, Phys. Rev. Lett **100**, 106402 (2008).

[32] A. H. C. Neto, Phys. Rev. Lett **86**, 4382 (2001).

[33] L. Fu and C. L. Kane, Phys. Rev. Lett **100**, 096407 (2008)

[34] In the review process of our paper after the completion of our work, we became aware of the following presentation: Sunseng Pyon *et al.*, in ICNSCT2011 (International conference on novel superconductivity in Taiwan): http://www.phys.sinica.edu.tw/~ICNS2011/download/abstract/P089.pdf).

Figure captions

Fig. 1 (Color online) (a) Lattice structure of $IrTe_2$. (b) Temperature-dependent magnetic susceptibility for Pd_xIrTe_2 ($0 \le x \le 0.03$) in H=2 T. (c) Temperature-dependent resistivity for Pd_xIrTe_2 ($0 \le x \le 0.04$) (normalized at 300 K). (d) Temperature-dependent magnetic susceptibility for $Ir_{1-y}Pd_yTe_2$ ($0 \le y \le 0.05$) in H=2 T. (e) Temperature-dependent resistivity for $Ir_{1-y}Pd_yTe_2$ ($0 \le y \le 0.07$) (normalized at 300 K). Black and red arrows indicate the cooling and heating processes, respectively.

Fig. 2 (Color online) (a) Electron diffraction pattern of $IrTe_2$ at 284 K. (b) Electron diffraction pattern of $IrTe_2$ at 84 K. (c) Reciprocal lattice of $IrTe_2$ at 84 K. Big balls represent the fundamental lattice, and small balls correspond to the superlattice. (d) The charge susceptibility $\chi(\vec{q})$ along L' (1/2, 0, -1/2)-Γ-L(0, 1/2, 1/2). The dominating peak is at $\vec{q}$=(~1.1/5, 0, ~-1.1/5) (red arrow). Black solid circles are the data calculated without SO coupling, and blue circles represent the one with SO coupling. (e) Inner and (f) outer Fermi surfaces of $IrTe_2$.

Fig. 3 (Color online) (a) Temperature-dependent superconducting (SC) shielding (zero-field cooled: ZFC) and Meissner (field cooled: FC) fraction data for Pd_xIrTe_2 ($0.02 \leq x \leq 0.1$) in H=10 Oe. (b) Temperature-dependent resistivity for Pd_xIrTe_2 ($0.02 \leq x \leq 0.1$) (normalized at 3.5 K). (c) Temperature-dependent SC fraction data for $Ir_{1-y}Pd_yTe_2$ ($0.03 \leq y \leq 0.07$), H=10 Oe. (d) Temperature-dependent resistivity for $Ir_{1-y}Pd_yTe_2$ ($0.03 \leq y \leq 0.07$) (normalized at 3.5 K). (e) Magnetic hysteresis loop for $Pd_{0.03}IrTe_2$ at 2 K. (f) Magnetic hysteresis loop for $Ir_{0.95}Pd_{0.05}Te_2$ at 1.8 K.

Fig. 4 (Color online) (a) Electronic phase diagram of Pd_xIrTe_2 (circles) and $Ir_{1-y}Pd_yTe_2$ (diamonds). Blue symbols correspond to the DW transition temperatures, and red symbols represent the superconducting transition temperatures. Open symbols indicate that the transition temperatures may be below our minimum available temperature.

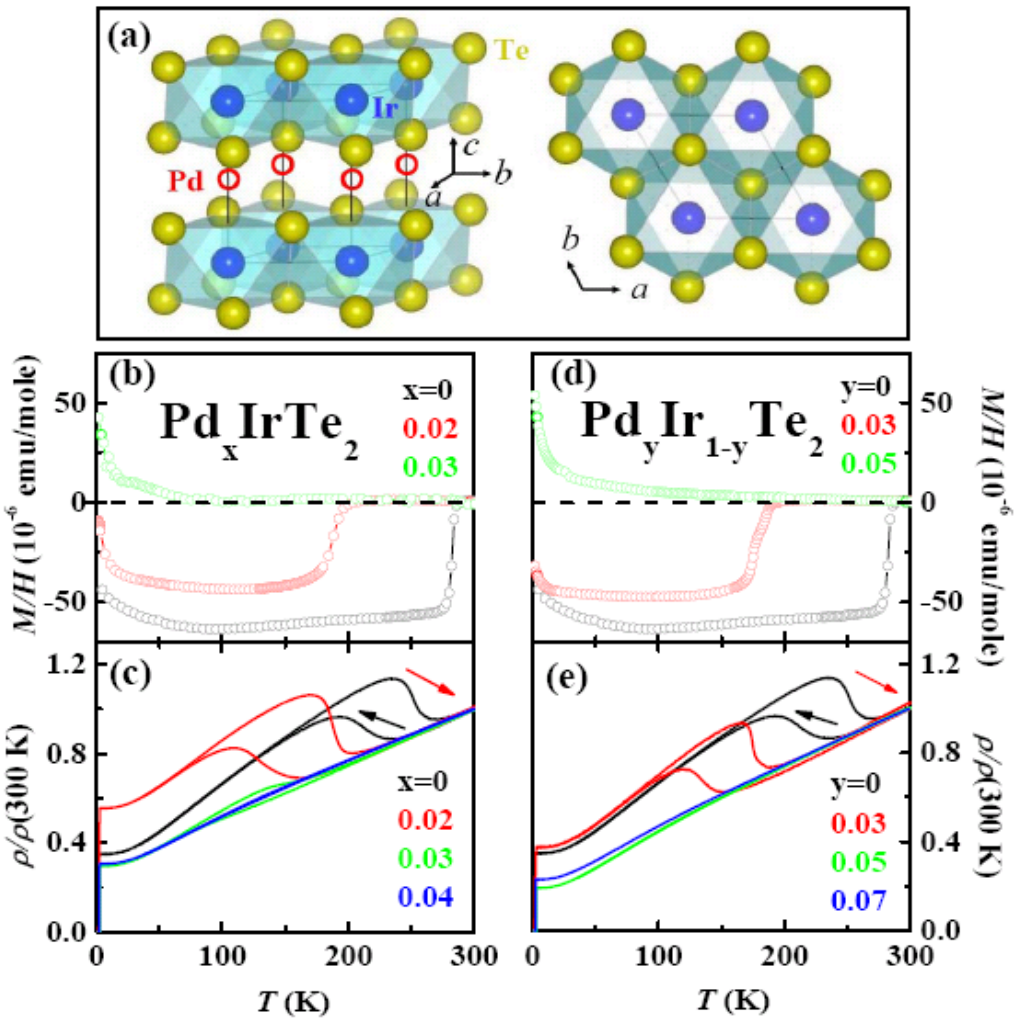
(a)
Te
Ir
Pd
c
b
a
b
a
(b)
Pd_xIrTe_2
x=0
0.02
0.03
M/H (10^-6 emu/mole)
50
0
-50
(c)
ρ/ρ(300 K)
1.2
0.8
0.4
0.0
x=0
0.02
0.03
0.04
0
100
200
300
T (K)
(d)
Pd_yIr_1-yTe_2
y=0
0.03
0.05
(e)
y=0
0.03
0.05
0.07

Fig 1

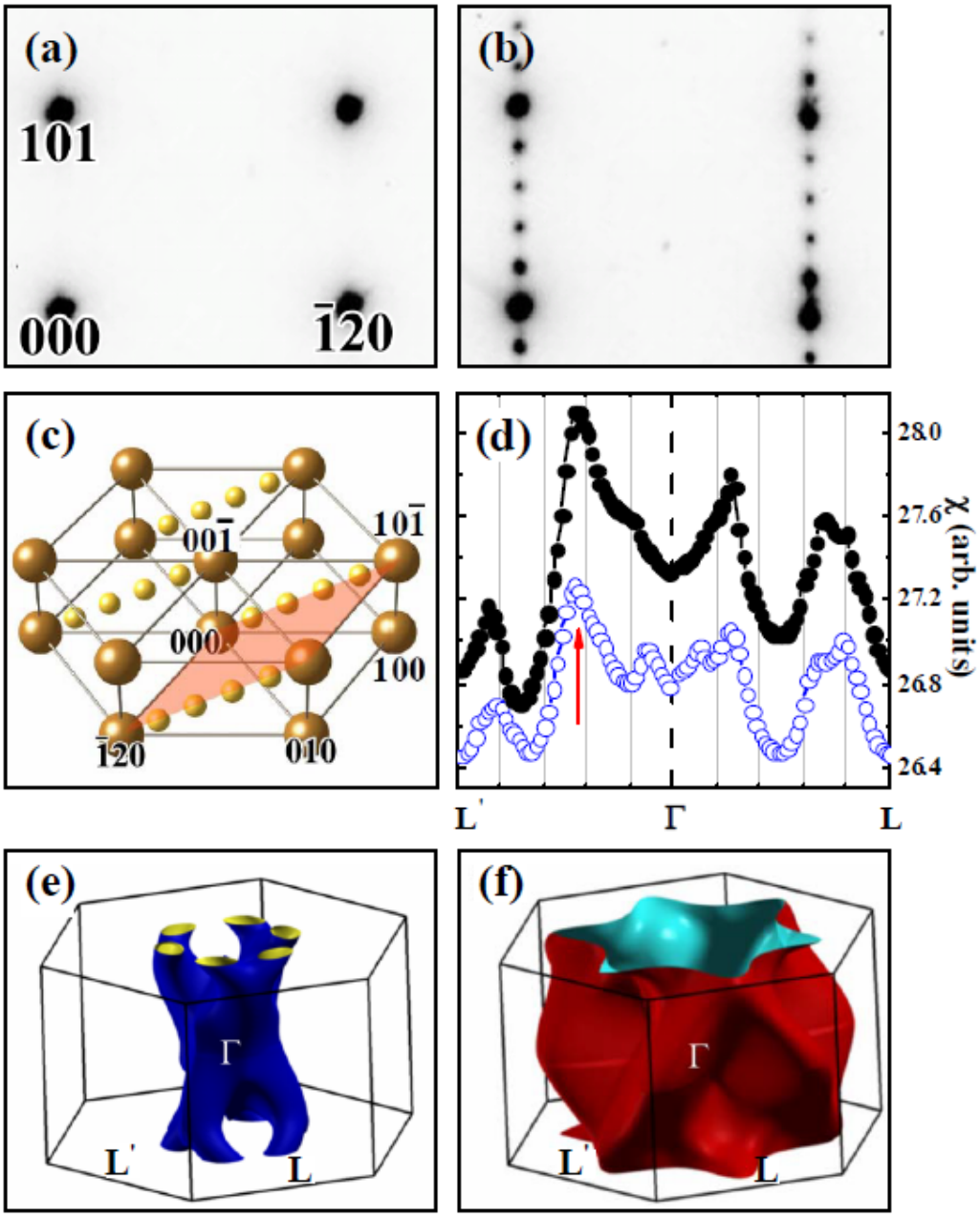
(a)
101
000
$\bar{1}20$
(b)
(c)
$00\bar{1}$
$10\bar{1}$
000
100
$\bar{1}20$
010
(d)
28.0
27.6
27.2
26.8
26.4
χ (arb. units)
L'
Γ
L
(e)
Γ
L'
L
(f)
Γ
L'
L

Fig 2

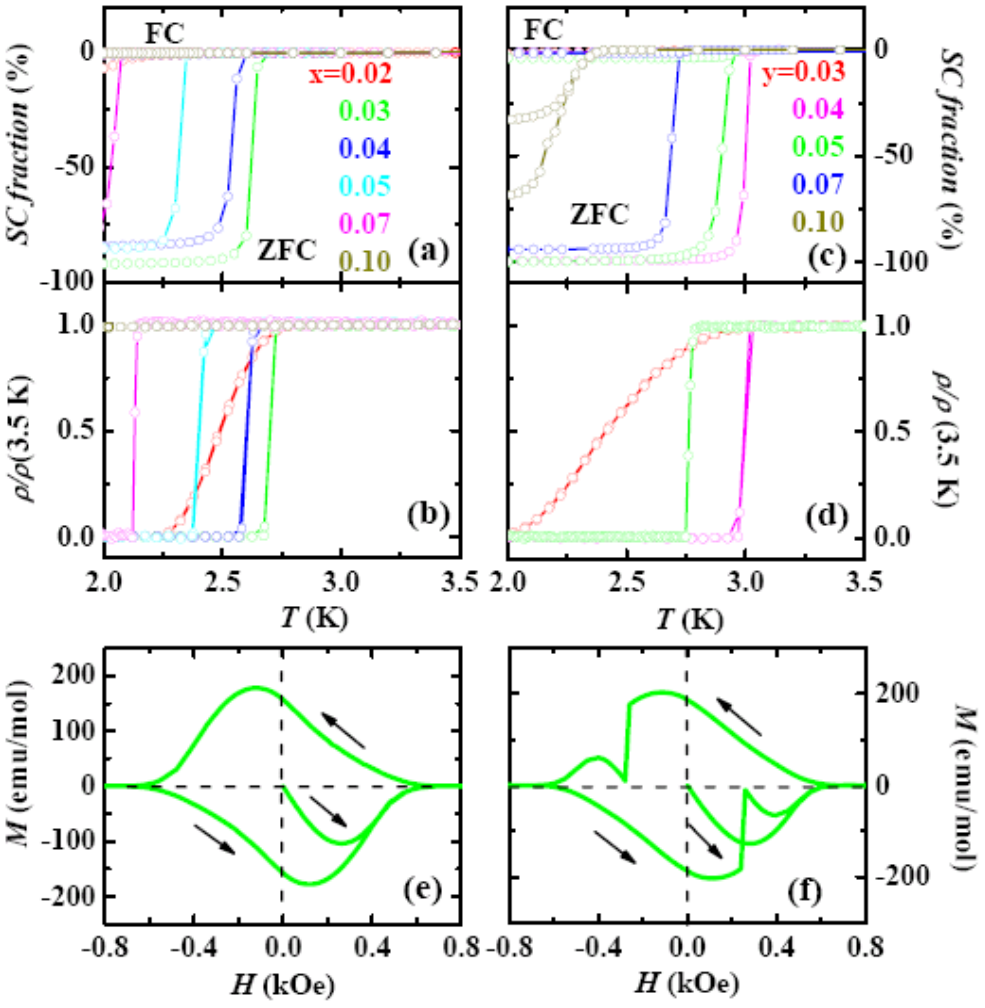
FC
ZFC
x=0.02
0.03
0.04
0.05
0.07
0.10
(a)
(b)
(c)
(d)
(e)
(f)
y=0.03
0.04
0.05
0.07
0.10
SC fraction (%)
ρ/ρ(3.5 K)
T (K)
M (emu/mol)
H (kOe)

Fig 3

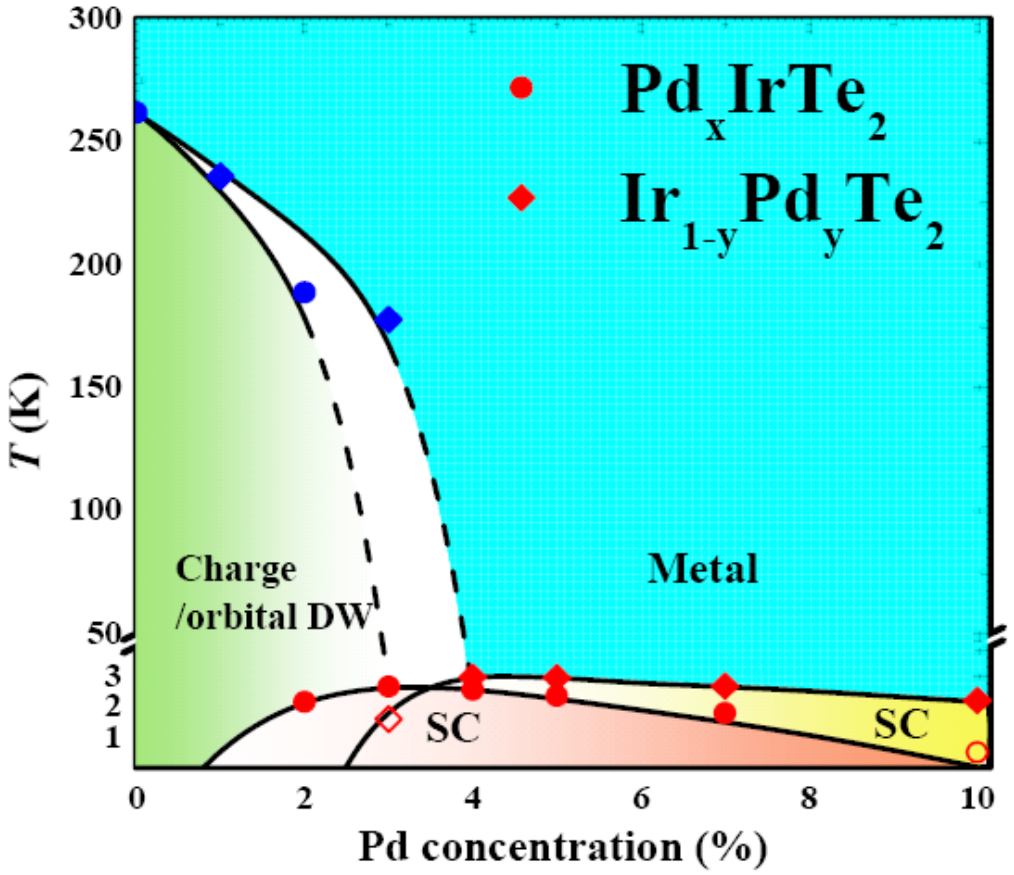
Pd_xIrTe_2
Ir_1-yPd_yTe_2
Charge
/orbital DW
Metal
SC
SC
T (K)
300
250
200
150
100
50
3
2
1
0
2
4
6
8
10
Pd concentration (%)

Fig 4